

## EXTRAPLANAR H II REGIONS IN SPIRAL GALAXIES. I. LOW-METALLICITY GAS ACCRETING THROUGH THE DISK-HALO INTERFACE OF NGC 4013

J. CHRISTOPHER HOWK,<sup>1,2</sup> KATHERINE M. RUEFF,<sup>1</sup> NICOLAS LEHNER,<sup>1</sup> CHRISTOPHER B. WOTTA,<sup>1</sup> KEVIN CROXALL,<sup>3,4</sup> AND BLAIR D. SAVAGE<sup>5</sup>

<sup>1</sup>*Department of Physics, University of Notre Dame, Notre Dame, IN 46556, USA*

<sup>2</sup>*Instituto de Astrofísica, Pontificia Universidad Católica de Chile, Santiago, Chile*

<sup>3</sup>*Department of Astronomy, The Ohio State University, Columbus, OH 43210, USA*

<sup>4</sup>*Illumination Works LLC, 5550 Blazar Parkway #150, Dublin, OH 43017, USA*

<sup>5</sup>*Department of Astronomy, University of Wisconsin, Madison, Madison, WI 53706, USA*

### ABSTRACT

The interstellar thick disks of galaxies serve as the interface between the thin star-forming disk, where feedback-driven outflows originate, and the distant halo, the repository for accreted gas. We present optical emission line spectroscopy of a luminous thick disk H II region located at  $z = 860$  pc above the plane of the spiral galaxy NGC 4013 taken with the Multi-Object Double Spectrograph on the Large Binocular Telescope. This nebula, with an H $\alpha$  luminosity  $\sim 4 - 7$  times that of the Orion nebula, surrounds a luminous cluster of young, hot stars that ionize the surrounding interstellar gas of the thick disk, providing a measure of the properties of that gas. We demonstrate that strong emission line methods can provide accurate measures of relative abundances between pairs of H II regions. From our emission line spectroscopy, we show that the metal content of the thick disk H II region is a factor of  $\approx 2$  lower than gas in H II regions at the midplane of this galaxy (with the relative abundance of O in the thick disk lower by  $-0.32 \pm 0.09$  dex). This implies incomplete mixing of material in the thick disk on small scales (100s of parsecs) and that there is accretion of low-metallicity gas through the thick disks of spirals. The inclusion of low-metallicity gas this close to the plane of NGC 4013 is reminiscent of the recently-proposed “fountain-driven” accretion models.

*Keywords:* galaxies: ISM – galaxies: abundances – galaxies: individual (NGC 4013)

### 1. INTRODUCTION

The continued formation of stars in a massive, Milky Way-like galaxy requires the addition of mass into the system from the intergalactic medium (IGM) to replace that consumed by star formation (e.g., Kennicutt 1983; Bauermeister et al. 2010; Fraternali & Tomassetti 2012). The timescales for IGM matter to reach a star forming disk may be very long, and the processes by which it gets there are quite varied. This is especially true for higher-mass galaxies, where any accreted gas is expected to be heated as it interacts with the extended coronal gas ( $T \approx T_{\text{vir}} \gtrsim 10^6$  K, the virial temperature of the galaxy). Once heated, the accreted gas is incorporated into the extended gaseous halo – and hence unavailable for star formation – until such time as it can cool and be deposited into the central star forming regions. However, there are significant questions about how effectively the halo of a Milky Way-like galaxy can cool on its own (i.e., the halo has a “stability problem” in that it may be largely stable against cooling Binney et al. 2009).

Recent models have invoked novel approaches to stimulating the cooling of coronal gas, providing a potential

new path to tapping this extensive reservoir of matter to fuel star formation. These take the form of “feedback-induced” or “fountain-induced” cooling (Marinacci et al. 2010, 2012; Fraternali 2017). In these models, metal-rich material ejected from the disk to large heights,  $z$ , above the plane of a galaxy mixes with the coronal material. The mixing of cold, metal-rich gas into the coronal matter provides the necessary ingredients for enhanced cooling. Such a mechanism could also be at play with material ejected through a “galactic bore” or hydraulic jump near spiral arms (e.g., Martos & Cox 1998) or perhaps even through the stimulation of cooling by high velocity clouds (Gritton et al. 2017). Thus, the galactic fountain or other mechanisms that eject disk material may be important to fueling the next generation of star formation.

Disk galaxies often exhibit signatures of recently-ejected disk material from either an active galactic fountain or other processes. A large fraction (Howk & Savage 1999) of nearby galaxies have thickened, rotating distributions of gas and dust several kiloparsecs thick (e.g., Rand et al. 1990; Dettmar 1990; Howk & Savage 2000; Fraternali et al. 2001; Heald et al. 2006; Zschaech-

ner & Rand 2015; Boettcher et al. 2016; Bizyaev et al. 2017) that can serve as boundary layers between the thin disks and hot halos. These “interstellar thick disks” are complex – with molecular, neutral, and ionized gas at a broad range of temperatures detectable in emission and absorption (García-Burillo et al. 1999; Rueff et al. 2013; Zschaechner & Rand 2015) – and have extents characterized by exponential scale heights of up to a few kiloparsecs. Much of the matter making up interstellar thick disks may be circulating through the first few kpc above the disk plane as part of a “galactic fountain,” carrying material upward for  $\sim 100$  Myr before it returns (Shapiro & Field 1976; Bregman 1980), or perhaps ejected as part of a hydraulic jump caused by shocks as gas falls into the potential well of a spiral arm (Martos & Cox 1998). This metal-rich disk material may supply the conditions needed to spur the cooling of coronal material. However, to date there has not been a straightforward path to testing for the presence of cooled coronal matter in the thick disk. Some studies have argued the rotational lag of the thick disk gas may indicate the presence of infalling gas (Fraternali & Binney 2006, not necessarily from the corona), although there may be other explanations for the lag (Struck & Smith 2009). Dust-to-gas indicators may provide a method of assessing the contribution from infalling matter to the thick disk (Peek et al. 2009; Howk 2012).

As part of their studies of gas in the “disk-halo interface<sup>1</sup>,” several groups have noted the presence of extraplanar H II regions far from the planes of edge-on galaxies (Walterbos 1991; Howk & Savage 2000; Tüllmann et al. 2003; Rueff et al. 2013; Stein et al. 2017). In some cases these include stars formed *in situ* (Howk et al. 2018), likely from the dense gas that is often seen threading the thick disk (Howk & Savage 1999, 2000; Rueff et al. 2013). No matter where they formed, the massive stars ionize and energize the surrounding thick disk gas to produce these extraplanar nebulae. The emission lines from these H II regions can be used as a probe of the gas in the thick disk, allowing us to study its metallicity (e.g., Tüllmann et al. 2003; Stein et al. 2017). The gas-phase abundance or metallicity of thick disk gas can be an indicator of its origins: gas dominated by outflows from the disk will have disk-like metallicities, while material accreting from the corona or even directly from the IGM will have a much lower metal content. Thus, these thick disk nebulae allow us to ask fundamental

questions about the nature of the baryon cycle in spiral galaxies.

There are a few existing measurements of abundances in thick disk H II regions, with a mix of results for their abundances relative to the disks of their host galaxies. Tüllmann et al. (2003) were the first to present convincing spectroscopy of extraplanar H II regions, in this case in the dwarf galaxy NGC 55. The two extraplanar H II regions in this galaxy (found to heights approaching  $z \approx 2$  kpc) are somewhat more enriched than the disk gas.<sup>2</sup> Recently, Stein et al. (2017) have provided new measurements of abundances in a total of three extraplanar H II regions in the galaxies NGC 3628 and NGC 4522 (at distances of  $1.4 \lesssim z \lesssim 3.0$  kpc from the midplane). These nebulae have abundances mostly consistent with their host galaxies, as expected given their likely origin in the tidally- or ram pressure-stripped material seen in H I maps of these galaxies (Wilding et al. 1993; Kenney et al. 2004). These are thus reminiscent of the H II regions in the outer disk / tidal material studied by Werk et al. (2011).

This is the first in a series of papers discussing the nature of extraplanar H II regions in edge-on spiral galaxies. Here we focus on abundance measurements in an extraplanar H II region located firmly within the interstellar thick disk of the edge-on galaxy NGC 4013. This nebula was briefly discussed by Rueff et al. (2013) as part of our study of the thick disk interstellar medium (ISM). It lies at a height of  $z = 860$  pc above the plane, within an interstellar thick disk that seems to be strongly influenced by an active galactic fountain (Howk & Savage 1999; Rueff et al. 2013). This region of the thick disk shows H I 21-cm emission from a warm neutral medium (Zschaechner & Rand 2015), H $\alpha$  emission from the diffuse ionized gas (DIG; Rand 1996; Rueff et al. 2013), as well as CO emission (García-Burillo et al. 1999) and dust absorption (Howk & Savage 1999; Rueff et al. 2013) from a cold neutral medium. Thus, the placement of this nebula allows us to probe the mixing of metals in a region typical of fountain-fed thick disks in spiral galaxies. A companion paper, Howk et al. (2018) (hereafter Paper II), describes the stars responsible for ionizing the nebula and the physical ingredients required to explain their *in situ* formation in the thick disk.

We discuss our emission line spectroscopy of the extraplanar H II region in §2, including our observations, data reduction, and emission line intensities. We use these observations to assess the abundance of this ex-

<sup>1</sup> We typically use the terms thick disk and disk-halo interface interchangeably to describe the interstellar material within the first few kpc above that largely co-rotates with the underlying disk of a galaxy.

<sup>2</sup> This conclusion is different than the original conclusions of Tüllmann et al. (2003), who were hampered by the diagnostics available at the time. See the details in §5.

traplanar nebula relative to that of gas in the thin disk in §3, including a detailed discussion of our approach to estimating the relative abundance. In §4 we discuss our derived metallicity offset for the thick disk H II region and the implications for mixing in NGC 4013. We discuss this measurement in the context of existing measurements from extraplanar H II regions and Milky Way halo clouds in §5, and we summarize our principal conclusions in §6. Throughout we assume a distance  $D = 17.1 \pm 1.7$  Mpc to NGC 4013 (equivalent to a distance modulus  $31.17 \pm 0.10$  mag). This is the mean distance to the galaxy group with which NGC 4013 is associated, group 102 from the catalog of Tully et al. (2008).

## 2. EMISSION LINE SPECTROSCOPY OF THE EXTRAPLANAR NEBULA NGC 4013 EHR1

We take advantage of an extraplanar H II region (EHR) to probe the origins of gas in the thick disk of the edge-on spiral galaxy NGC 4013. The upper left panel of Figure 1 shows an H $\alpha$  image of part of NGC 4013 from Rueff et al. (2013). This nebula – NGC 4013 EHR1 – is marked by the red circle. EHR1 has a luminosity  $\sim 4 - 7$  times that of the Orion nebula at a projected height above the midplane  $z = 860$  pc and projected radial distance of  $R \sim 2.5$  kpc from the galaxy’s center. This section describes the properties of our low-resolution optical long-slit spectra of NGC 4013 EHR1 and two reference regions in the thin disk using one of the Multi-Object Dual Spectrographs (MODS) on the Large Binocular Telescope (LBT). The final extracted spectrum of EHR1 is shown in the bottom panel of Figure 1, and select emission line ratios for NGC 4013 EHR1 (and the two disk regions) derived from these data are compared with a sample of extragalactic H II regions from the local universe (Bresolin et al. 2009; Berg et al. 2015; Croxall et al. 2015; Croxall et al. 2016) in the upper right panel. The emission line spectrum of EHR1 is characteristic of H II regions found in the disks of spiral galaxies. This and its radial velocity, which is consistent with that of the local diffuse ionized gas, demonstrate that EHR1 is an H II region in the thick disk of NGC 4013.

### 2.1. Observations and Basic Reduction

We used the first of the MODS instruments (MODS1) installed on the LBT to obtain spectra of both NGC 4013 EHR1 and the two reference H II regions in the disk of NGC 4013 (Figure 1). The coordinates, projected radial distance from the galaxy center,  $R$ , and  $z$ -heights of the three nebulae are listed in Table 1. The MODS instruments are described by Pogge et al.

**Table 1.** Observed NGC 40 H II Regions

Name	RA (J2000)	Dec (J2000)	$R$ (kpc)	$z$ (pc)
EHR1	11 58 33.2	+43 57 11.85	2.5	860
disk 1	11 58 33.7	+43 57 00.86	2.3	$\approx 0$
disk 2	11 58 34.2	+43 57 03.88	2.9	$\approx 0$

(2010), and examples of MODS1 spectroscopy applied to H II region abundances can be found in the CHAOS papers (Berg et al. 2015; Croxall et al. 2015; Croxall et al. 2016).

MODS1 is a double spectrograph with separate blue and red channels. Both channels are used simultaneously, and the light is split by a dichroic with a crossover at  $\lambda \sim 5500$  Å. We adopted the standard set-up of the instrument, with the G400L grating (400 lines  $\text{mm}^{-1}$ ) in the blue and the G670L (250 lines  $\text{mm}^{-1}$ ) grating in the red. In this configuration, MODS provides wavelength coverage over  $3200 \lesssim \lambda \lesssim 10000$  Å, which is sampled after reduction at  $0.5$  Å per pixel. All of our observations used the  $1''$ -wide longslit mask, which is a sequence of five slits of length  $1'$  aligned end-to-end with a few arc-sec gaps between them. This has no practical effect for our work compared with a contiguous longslit, and we will discuss this mask as if it were a traditional single longslit. With our  $1''$  slit width, both spectrograph channels give a spectral resolution  $R \sim 1200$ .

We observed NGC 4013 EHR1 on 2012 June 15 and the disk H II regions on 2015 January 20. In the case of EHR1 the slit was aligned at the parallactic angle, and the object observed for  $3 \times 20$  minutes. For the disk observations, the slit was placed along the disk of NGC 4013 (at PA  $64^\circ 2' E$  of N), which was within  $10^\circ$  of the parallactic angle during those observations. The disk was observed for  $3 \times 20$  minutes. The seeing in both cases was under  $1''$  and both observations were obtained in photometric conditions.

### 2.2. Data Reduction and Spectral Extraction

The basic reduction and spectral extraction is done using the MODS reduction pipeline<sup>3</sup> developed by K. Croxall and based on the XIDL code<sup>4</sup>. The code has

<sup>3</sup> The MODS reduction pipeline was developed by Kevin Croxall with funding from NSF Grant AST-1108693. Details can be found at <http://www.astronomy.ohio-state.edu/MODS/Software/modsIDL/>.

<sup>4</sup> The XIDL code of J.X. Prochaska is available at <https://github.com/profxj/xidl>.

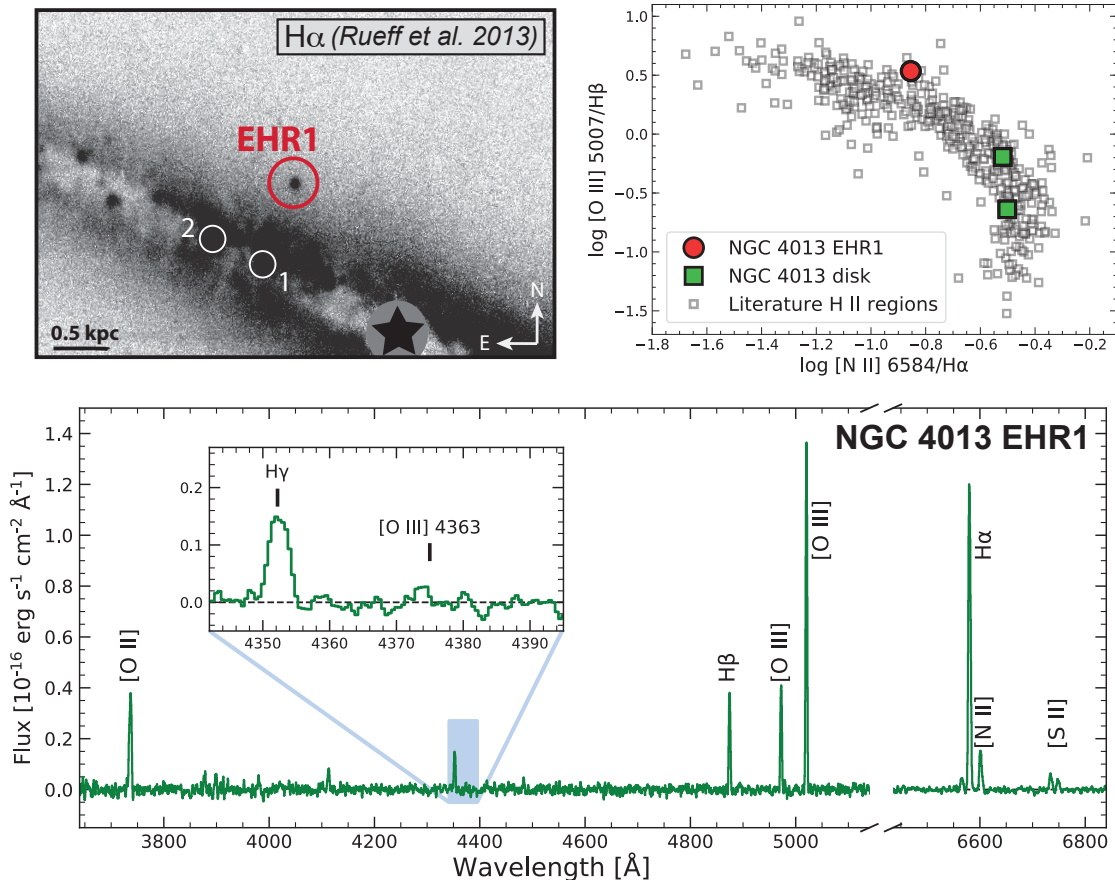


**Figure 1.** Montage of results on NGC 4013 EHR1. *Top left:* WIYN  $H\alpha$  image of the edge-on spiral galaxy NGC 4013 [Rueff et al. \(2013\)](#) showing the location of the extraplanar H II region EHR1 as well as the two disk H II regions used to define the disk reference abundance. NGC 4013 EHR1 is seen at a height  $z = 860$  pc. (The black star hides mis-subtracted emission about a very bright foreground Milky Way star.) *Top right:* Observed emission line ratios for EHR1 compared with literature measurements of H II regions in the disks of spiral galaxies ([Berg et al. 2015](#); [Croxall et al. 2015](#); [Croxall et al. 2016](#); [Bresolin et al. 2009](#)). These ratios for EHR1 are similar to those seen in normal H II regions. Combined with its velocity, which is consistent with the diffuse ionized gas emission in this region of NGC 4013, this identifies EHR1 as an H II region in the thick disk of this galaxy. *Bottom:* Partial LBT/MODS1 spectrum of EHR1 with several of the strongest lines identified. The inset shows the spectral region encompassing  $H\gamma$  and the undetected auroral [O III] 4363 Å transition (the shaded blue box shows this region in the larger spectrum).

been applied and briefly described as part of the CHAOS project ([Berg et al. 2015](#); [Croxall et al. 2015](#); [Croxall et al. 2016](#)), and we refer the reader particularly to [Berg et al. \(2015\)](#) for the most detailed description. Following those works we assume a 2% uncertainty in the flux calibration, adding this in quadrature to the errors associated with general Poisson noise, read noise (negligible), sky and background subtraction uncertainties.

We extracted the spectrum for NGC 4013 EHR1 using a  $1''.5$  extraction box, while we used a  $2''.0$  box for the disk H II regions in order to account for all of the flux. In each case we extracted equally-sized background spectra on either side of the objects of interest. One of the key components of the data reduction is assessing and removing the background from the emission line spec-

tra of the H II regions. This is particularly important for EHR1, for which the long-slit spectra include contributions from the nebula as well as from both from the old stellar population of the thick disk and bulge (continuum) plus the diffuse ionized gas (DIG) of the thick disk (emission lines). The DIG emission line spectrum is quite different from the nebular emission from EHR1 itself, with ratios  $[N II]/H\alpha \approx 1$ , for example, compared with a ratio of  $\approx 0.13$  for the H II region. Thus proper background subtraction is important, as while the  $H\alpha$  emission from the DIG is much fainter (only  $\sim 13\%$ ) than that of EHR1, the forbidden line strengths can contribute significantly to the uncorrected spectrum (with DIG lines matching those from EHR1).



We have tested the background subtraction for EHR1 in two ways; both give indistinguishable results. In the first approach, we assume a fully-empirical background, using the geometric mean of the spectra from regions immediately adjacent to the extraction box for EHR1. These spectra were extracted just as those of EHR1. We use a geometric mean under the assumption that the DIG and stellar background light have exponential decays with height. As shown in Figure 2, the resulting background spectrum is a very good match to the shape and intensity of the continuum light underlying EHR1. There is a slight residual continuum that we remove with a low-order polynomial (the residuals are roughly flat and  $\lesssim 10\%$  of the local flux). This may arise from slightly different extinction or stellar populations, or if the use of the geometric mean of the background regions results in a slight departure from the true stellar populations underlying EHR1.

The second approach uses a full spectral fit of both the EHR1 spectrum and separately the geometric mean of the two background region spectra (on either side of the nebula) using the penalized pixel fitting (pPXF) software of Cappellari (2017). In this approach, we fit composite stellar models and nebular emission lines to the spectrum over the wavelength range  $3500 \lesssim \lambda \lesssim 7500$  Å. The wavelength range is set by the useful range of the MILES spectral libraries (Sánchez-Blázquez et al. 2006) that we adopt to construct the composite spectrum. While we fit the emission lines as part of the process, this is done only to allow for their effects on the fitted background stellar spectra. We subtract the pPXF-derived stellar flux models from the EHR1 and background spectra, leaving a pure emission line spectrum from the nebula and DIG. We then subtract the background DIG emission line spectrum from that observed toward EHR1.

These two approaches give final emission line spectra for EHR1 that are indistinguishable. We adopt the direct empirical background moving forward. The background assessment for the two disk H II regions followed a similar approach.

### 2.3. Emission Line Measurements

We measured the intensities of the emission lines by fitting the full spectrum with a Gaussian emission line model, returning the velocities, velocity dispersions, and intensity for all potential lines of interest. We generally forced the dispersions of lines from the same ion to be the same. Within the same spectrograph channel, the central velocities of the collisionally-excited metal lines were tied in the fitting process, as were those of the Balmer lines. Once the emission lines were fitted, we

also use the central velocities and dispersions to measure emission line intensities via direct integration of the lines.

For NGC 4013 EHR1 and the reference region disk 1, the line profiles were well fit by our assumed Gaussian models. The same is not true for the disk 2 region, which shows substructure in the lines associated with the structure in the nebular emission as projected onto the slit. There is also some evidence that slit losses for the disk 2 spectrum may be more significant in the red than the blue, as the line shapes are not in great agreement between the spectrographs, and there is a slight velocity offset between the two channels that is not seen in the disk 1 spectra. This is also reflected in the comparison of the integrated and fitted line intensities, which are quite similar for EHR1 and disk 1, but have larger discrepancies in the disk 2 spectrum (seemingly due to the non-Gaussian line profiles in the disk 2 spectrum). We feel the integrated lines are more representative of the true fluxes for at least the reference disk 2 region, and we adopt those throughout. Given the peculiarities of the disk 2 spectra, as well as the coincidence in projected radial distance between EHR1 and disk 1, we favor the results from disk 1 and will use this object as our main reference against which to judge the properties of EHR1. We note that the velocities of the reference disk 1 ( $v_{\text{disk 1}} = 698 \pm 25$  km s<sup>-1</sup> heliocentric) and EHR1 ( $v_{\text{disk 1}} = 720 \pm 25$  km s<sup>-1</sup>) are also similar, which could indicate they arise from similar locations in the galaxy.

We assess the foreground extinction toward each nebula by comparing the ratio of H $\beta$  to H $\gamma$  assuming  $T_e \approx 10^4$  K. We do this rather than the more typical H $\alpha$ /H $\beta$  ratio in order to avoid comparisons across the dichroic break. For disk 2, in particular, we subsequently adjust the scale of the red spectra such that H $\alpha$ /H $\beta$  is in agreement with expectations. We have experimented with using the H $\alpha$ /H $\beta$  ratio to determine the extinction, which always leads to larger extinction values; however, our abundance results are insensitive to this choice, as the emission line ratios we use to derive abundances typically use line pairs close in wavelength (3.1).

The resulting extinction-corrected line intensities relative to H $\beta$  and the adopted color excesses,  $E(B - V)$ , for each nebula are given in Table 2. We expect that the Milky Way contributes  $< 0.02$  mag to these color excesses (Schlafly & Finkbeiner 2011).

### 2.4. Physical Conditions of the Thick Disk H II Region

Our spectra provide some constraints on the physical properties of the thick disk H II region NGC 4013

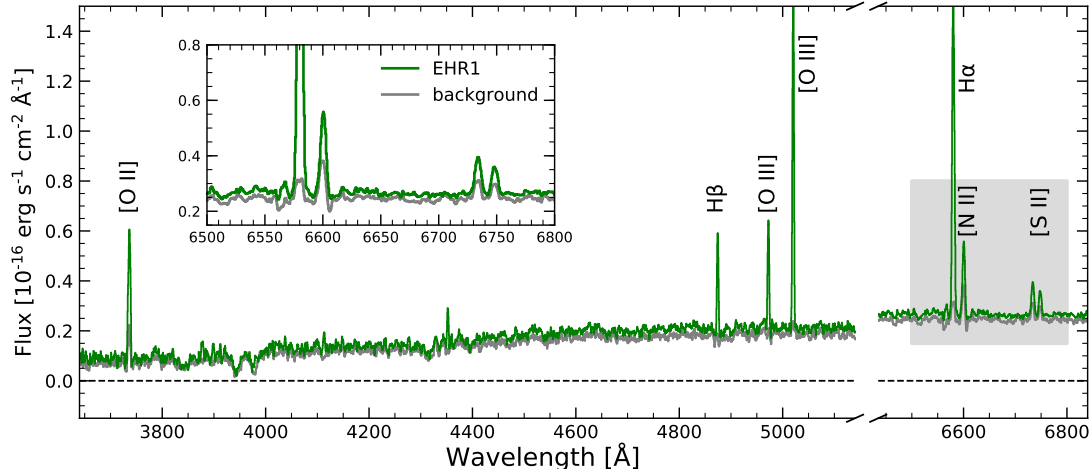


**Figure 2.** A comparison of the spectrum extracted toward EHR1 (green) with our estimate of the background light (grey) based on a combination of spectra extracted on either side of our target. The spectrum toward EHR1 includes line emission from the nebula EHR1 itself, line emission from the DIG, and continuum emission from the bulge and thick disk light in this direction. The background spectrum is difficult to see in most of the spectrum given the good agreement between the continuum emission in the target and background spectra. The stellar continuum emission from the stars powering EHR1 itself is not expected to be detected (it has  $V \sim 23.7$  mag; see Paper II), nor is it seen. The strong absorption lines seen in both the background and EHR1 directions are from the old stellar populations in these directions; Ca II  $\lambda$ ,  $\lambda 3933$ ,  $3968$  are the most prominent. The inset shows the region around H $\alpha$ , including the forbidden [N II] and [S II] transitions, in order to demonstrate the differing contributions the background DIG makes to these lines. A slight residual flux difference is seen between the object and background spectra, which we remove by subtracting a low-order polynomial fit to the residual continuum.

**Table 2.** Extinction-corrected Emission Line Intensities

Line	$100 \times I_{\lambda}/I_{H\beta}$		
	EHR1	disk 1	disk 2
[O II] 3727	$226.9 \pm 6.9$	$254.2 \pm 10.2$	$277.8 \pm 5.6$
H $\gamma$ 4341	$47.0 \pm 2.2$	$46.6 \pm 2.7$	$46.6 \pm 1.0$
[O III] 4364	$< 6.1$	$< 6.9$	$< 1.6$
H $\beta$ 4861	$\equiv 100.0$	$\equiv 100.0$	$\equiv 100.0$
[O III] 4960	$107.3 \pm 2.7$	$6.3 \pm 1.5$	$19.6 \pm 0.5$
[O III] 5008	$342.3 \pm 7.1$	$24.0 \pm 1.6$	$63.5 \pm 1.3$
[N II] 6549	$12.3 \pm 0.9$	$29.3 \pm 0.7$	$29.6 \pm 0.6$
H $\alpha$ 6564	$289.6 \pm 5.9$	$285.8 \pm 5.7$	$286.8 \pm 5.7$
[N II] 6585	$40.5 \pm 1.3$	$91.6 \pm 1.9$	$86.7 \pm 1.7$
[S II] 6718	$16.3 \pm 1.0$	$35.9 \pm 0.8$	$40.9 \pm 0.8$
[S II] 6732	$9.0 \pm 1.0$	$25.0 \pm 0.6$	$29.0 \pm 0.6$
$E(B - V)$ (mag)	$0.22 \pm 0.07$	$0.42 \pm 0.09$	$0.41 \pm 0.04$

NOTE—Upper limits are  $3\sigma$ . The intensity reported for the [O II] 3727 line is the sum of the two members of the [O II] doublet.

EHR1. For none of the three H II regions have we detected the weak temperature-sensitive auroral lines needed to derive their temperatures (e.g, [O III]  $\lambda 4363$  shown in the inset of Figure 1). Our non-detection of

[O III]  $\lambda 4363$  for EHR1 provides an electron temperature upper limit  $T_e([\text{O III}]) \lesssim 13,200$  K ( $3\sigma$ ). Many studies have found the temperatures and gas-phase oxygen abundances of H II regions are correlated; our temperature limit is characteristic of H II regions with  $\epsilon(\text{O}) \equiv 12 + \log(\text{O}/\text{H}) \gtrsim 7.7$ , assuming the correlation of López-Sánchez et al. (2012). This lower limit is well below the estimates of  $\epsilon(\text{O})$  for EHR1 we derive below (§3.2). Thus we are likely quite far from detecting the [O III]  $\lambda 4363$  emission.

The ratio [S II]  $\lambda 6717/\lambda 6731$  is consistent with the low-density limit of this diagnostic, placing an upper density limit  $n_e \leq 100$   $\text{cm}^{-3}$ . The H $\alpha$  luminosity of the nebula,  $L_{\text{H}\alpha} \geq (4.0 \pm 1.2) \times 10^{37}$  ergs  $\text{s}^{-1}$ , requires an H-ionizing photon production rate  $\log Q_0 \geq 49.4$  (units of photons  $\text{s}^{-1}$ ; Paper II). Thus EHR1 is a relatively luminous H II region, with an H $\alpha$  luminosity  $L_{\text{H}\alpha} \sim 4$ –7 times that of the Orion nebula<sup>5</sup>. The ionizing photon flux required to power this is equivalent to that of  $\sim 6$  O7 V stars (see Paper II). The H $\alpha$  emission is unresolved in our images ( $R_S \lesssim 33$  pc; Rueff et al. 2013). Using this radius, we derive a lower density limit assuming the

<sup>5</sup> We assess the Orion nebula luminosity based on the distance from Sandstrom et al. (2007) and integrated flux from Rumstay (1984).

nebula is a Strömgren sphere, providing overall limits of  $5 \leq n_e \leq 100 \text{ cm}^{-3}$ .

### 3. RELATIVE METALLICITY OF THE THICK DISK H II REGION

Given our non-detection of the auroral lines, we cannot derive “direct” gas-phase abundance estimates from our data. We must rely on the so-called “strong emission line” (SEL) techniques to estimate the gas-phase oxygen abundance. There are a variety of SEL scales available, which we take to include a method (e.g., the “O3N2 method”) and a specific calibration of that method (e.g., the calibration of the N2 method by Pettini & Pagel 2004). There can be significant systematic errors in SEL-based absolute metallicities,  $\epsilon(\text{O}) \equiv 12 + \log(\text{O}/\text{H})$ , for a given H II region, and the errors are different for each chosen scale. However, the *relative* metallicities of two H II regions,  $\Delta\epsilon(\text{O}) \equiv \epsilon(\text{O})_j - \epsilon(\text{O})_k$ , within a given scale are robust, as we demonstrate below (see also Kewley & Ellison 2008). For this reason, we focus on calculating the relative abundance of the H II region EHR1 compared with our reference nebulae in the disk. Thus, we are focusing on calculating abundance gradients or offsets rather than the absolute abundances.

#### 3.1. Choosing SEL Abundance Scales

There are a multitude of SEL scales available in the literature. Individual scales, even using the same method, can give different absolute abundances (Kewley & Ellison 2008; Curti et al. 2017). In this work, we make use of a limited set of abundance scales for determining the abundance offset between EHR1 and the disk of NGC 4013. We choose a set of scales based on their applicability to the current situation, focusing on those calibrated in the metallicity regime describing our objects (which all scales place in the range  $\epsilon(\text{O}) \approx 8.25$  to 8.80). We exclude from consideration those scales that are double-valued with turn-around points that are nearly coincident with the metallicities at which we appear to be working (e.g., the  $R_{23}$  method; Kewley & Ellison 2008).

In some cases, several calibrations of a given metallicity method (indicator) give good results that could be useable. However, we use only one calibration for each method in deriving our final results in order to minimize potentially correlated systematic issues across the calibrations. We have also avoided methods that rely on the [O II] 3727 lines given the large uncertainties in our extinction correction (although their adoption would not lead to a different result).

To choose which are the most appropriate scales for our purposes, we have assessed which scales provide robust measures of abundance offsets,  $\Delta\epsilon(\text{O})$ , analyzing 17

separate scales from the literature. For each scale we calculate  $\Delta\epsilon(\text{O})$  from direct method abundances for a sample of literature H II regions in spiral galaxies (Bresolin et al. 2009; Berg et al. 2015; Croxall et al. 2015; Croxall et al. 2016) and compare them with calculated offsets from each SEL scale. We calculate  $\Delta\epsilon(\text{O})_{\text{SEL}}$  for a sample of “low metallicity” H II regions (with direct abundances  $8.20 \leq \epsilon(\text{O}) \leq 8.50$ ) compared with a “high metallicity” sample (with  $8.50 \leq \epsilon(\text{O}) \leq 8.80$ ). These metallicity regimes bracket the abundance ranges predicted in an initial determination of the H II regions in NGC 4013. We compare the implied offsets derived using the SEL abundances with those from the direct methods to identify which SEL methods and calibrations give reliable results. We also assess the dispersion in the SEL offsets about the direct method results. In Table 3 we summarize the median discrepancies in  $\Delta\epsilon(\text{O})$  when comparing the SEL and direct results as well as the intrinsic dispersions for the scales we considered.

**Table 3.** Characteristics of SEL Metallicity Scales

Method	Calibration <sup>a</sup>	$\Delta\epsilon(\text{O})_{\text{SEL}} - \Delta\epsilon(\text{O})_{\text{Direct}}$	$\sigma_{\Delta\epsilon(\text{O})}$ <sup>b</sup>
Adopted scales for calculating $\Delta\epsilon(\text{O})$			
N2	PP04	+0.024	0.169
O3N2	M13	+0.010	0.155
O3	C17	-0.009	0.178
Reliable scales for calculating $\Delta\epsilon(\text{O})$			
N2	M13	+0.030	0.136
N2	C17	+0.002	0.148
N2O2	PMC09	-0.012	0.217
O3N2	C17	-0.024	0.176
O3O2	C17	+0.054	0.196
Less-reliable scales for calculating $\Delta\epsilon(\text{O})$			
N2	KK04	-0.016	0.216
N2	M08	-0.110	0.251
O3N2	PP04	-0.108	0.229
O3N2	M08	-0.188	0.349
O3N2	PMC09	-0.096	0.218
O3O2	M08	-0.081	0.359
O3	M08	-0.158	0.311
N2O2	B07	-0.070	0.169
N2O2	KD02	-0.046	0.244

<sup>a</sup> Calibration scale references – B07 (Bresolin 2007), C17 (Curti et al. 2017), KD02 (Kewley & Dopita 2002), KK04 (Kobulnicky & Kewley 2004), M08 (Maiolino et al. 2008), M13 (Marino et al. 2013), PP04 (Pettini & Pagel 2004), PMC09 (Pérez-Montero & Contini 2009)

<sup>b</sup> Dispersion in the  $\Delta\epsilon(\text{O})_{\text{SEL}} - \Delta\epsilon(\text{O})_{\text{Direct}}$  in dex.

Based on these results, we adopt the following SEL scales: the N2 scale from Pettini & Pagel (2004), the O3N2 scale of Marino et al. (2013), and the O3 scale of Curti et al. (2017). All three adopted scales provide have mean values of  $|\Delta\epsilon(\text{O})_{\text{SEL}} - \Delta\epsilon(\text{O})_{\text{Direct}}| \lesssim 0.03$  dex and dispersions in this quantity  $\approx 0.15$  to  $0.18$  dex. Table 3 gives the results of the above analysis for all 17 scales we considered. We break these down, showing the three scales we ultimately adopt, the scales we did not adopt but still considered reliable for such calculations, and those that were not appropriate for our uses. Our assessment of the appropriateness of the scales is based on measures beyond simply this table. For example, we rejected some of the scales because they show non-linear slopes in the relationship between the SEL and direct method abundances, with breaks in the relationships that do not bias too much the mean behavior of the indicators but might for the study of individual objects. We note that the methods that rely on [O II] tend to have large dispersions and  $\Delta\epsilon(\text{O})$  offsets generally.

An important take-away from our analysis is the SEL-based calculations of  $\Delta\epsilon(\text{O})$  are in fact quite consistent with one another and with the direct method results when using any of the scales deemed reliable in Table 3. The SEL and direct method calculations of  $\Delta\epsilon(\text{O})$  are, as expected, much more consistent than the results for the absolute abundances,  $\epsilon(\text{O})$ . The absolute abundances,  $\epsilon(\text{O})$ , can have systematic offsets of  $0.1 - 0.3$  dex in this range of metallicities, while the discrepancies in the relative abundance offsets,  $\Delta\epsilon(\text{O})$ , are more typically in the  $0.0 - 0.1$  dex range. Although we will apply a limited number of abundance scales to our determination of  $\Delta\epsilon(\text{O})$ , our final results are not particularly sensitive to the specific choice of scales from among those deemed reliable in Table 3.

### 3.2. Estimating the Relative Abundance $\Delta\epsilon(\text{O})$

We use a Monte Carlo approach based on the pyMCZ code (Bianco et al. 2016) to assess the posterior distribution functions of the abundances  $\epsilon(\text{O}) \equiv 12 + \log(\text{O}/\text{H})$  for each H II region and subsequently of  $\Delta\epsilon(\text{O}) \equiv \epsilon(\text{O})_{\text{EHR1}} - \epsilon(\text{O})_{\text{ref}}$  between EHR1 and the reference regions. This code uses Monte Carlo sampling of the input emission line intensity distributions to assess the posterior distribution functions of SEL abundances from a choice of abundance scales. In our approach, we sample the emission line intensities for a given H II region 4000 times (assuming a normal distribution with central values and dispersions given from measurements), calculating the extinction and gas-phase abundance implied by each sample. The net result is a posterior distribu-

tion of gas-phase oxygen abundances for each H II region from each SEL scale.

We consider the relative abundances of EHR1 with two disk H II regions shown in Figure 1, which we take to be representative of the disk as a whole. We calculate a posterior distribution for  $\Delta\epsilon(\text{O})$  in each scale by comparing the Monte Carlo samples of EHR1 with the randomly-ordered samples for the reference disk regions. An individual H II region will not lie directly on the calibrated relationship between SEL ratios and gas-phase abundance due both to errors in the emission line intensities, but also due to intrinsic differences in physical conditions and ionization states that are not accounted for in the SEL methodology. We account for this intrinsic scatter of individual H II regions about the mean SEL scales by adding normally-distributed random offsets when calculating  $\Delta\epsilon(\text{O})$  for each pair of Monte Carlo samples. The dispersions adopted for each SEL scale are drawn from Table 3. This source of uncertainty (typically  $\sim 0.15$  to  $0.20$  dex for reliable SEL scales) dominates over the propagated observational uncertainties ( $\sim 0.02$  to  $0.04$  dex). In addition, for each SEL scale we add a correction to the  $\Delta\epsilon(\text{O})$  values to account for the offsets between  $\Delta\epsilon(\text{O})$  derived from that scale compared with those derived from direct abundance measurements. We use the corrections summarized in Table 3. Because these are quite small for our adopted scales, they have only a small impact on the final result.

For each of the scales we have a posterior distribution,  $P_k[\Delta\epsilon(\text{O})]$ , describing the likelihood of the values of  $\Delta\epsilon(\text{O})$  between EHR1 and a reference nebula for each scale  $k$ . We have demonstrated that the relative gas-phase abundances,  $\Delta\epsilon(\text{O})$ , are robust in our adopted SEL scales, and we have no reason *a priori* to weight one scale more than another. Thus for a given reference nebula, we combine the results from each scale, deriving a posterior distribution for  $\Delta\epsilon(\text{O})$  with respect to each of the reference disk H II regions, creating a joint distribution,  $P[\Delta\epsilon(\text{O})]$ :

$$P[\Delta\epsilon(\text{O})] = \prod_k P_k[\Delta\epsilon(\text{O})],$$

which we evaluate numerically.

Figure 3 shows the individual distributions  $P_k[\Delta\epsilon(\text{O})]$  for our three adopted SEL scales as applied to the EHR1-disk 1 comparison (top panel) and EHR1-disk 2 comparison (bottom panel). Each panel also shows the joint distribution  $P[\Delta\epsilon(\text{O})]$  describing our final result (all PDFs are normalized). The individual and combined results are summarized in Table 4. Our final estimates of  $\Delta\epsilon(\text{O})$  for EHR1 compared with each



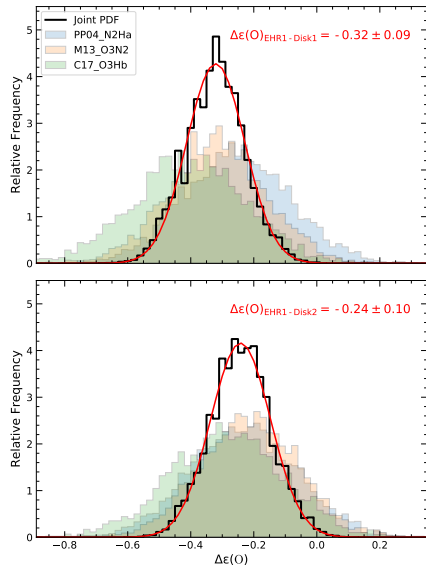


**Figure 3.** Probability density functions for the abundance offset of the thick disk H II region NGC 4013 EHR1 relative to the two reference regions in the disk. The top panel shows the results relative to the reference nebula disk 1, the bottom relative to disk 2. In both panels, the shaded distributions show the results for each of the three individual SEL scales used ( $P_k[\Delta\epsilon(\text{O})]$ ). The black histogram shows the joint PDF ( $P[\Delta\epsilon(\text{O})]$ ) combining the three scales, and the red line shows a Gaussian fit to the distribution. Our principal results are those relative to the reference nebula disk 1, as the data for the disk 2 nebula likely suffer from non-uniform slit losses.

reference region are based on the joint posterior distribution combining the three adopted SEL scales. Our favored results are those using only disk 1 as a reference:  $\Delta\epsilon(\text{O})_{\text{EHR1-disk1}} = -0.32 \pm 0.09$ . As the distributions are close to normally-distributed, this value is the mean of the distribution based on a Gaussian fit to the PDF with 68% confidence errors. If we consider disk 2 as the reference nebula we find  $\Delta\epsilon(\text{O})_{\text{EHR1-disk2}} = -0.24 \pm 0.10$ . Using the disk nebulae together as a joint reference yields  $\Delta\epsilon(\text{O})_{\text{EHR1-disk}} = -0.28 \pm 0.06$ . We emphasize that EHR1 has an abundance lower than both disk H II regions in every SEL scale we tested.

The ultimate  $\Delta\epsilon(\text{O})$  values are not overly sensitive to which set of scales we adopt. If we jointly apply all of the “reliable” scales from Table 3, we find  $\Delta\epsilon(\text{O})_{\text{EHR1-disk1}} = -0.28 \pm 0.05$ , and  $\Delta\epsilon(\text{O})_{\text{EHR1-disk2}} = -0.22 \pm 0.05$ , and jointly  $\Delta\epsilon(\text{O})_{\text{EHR1-disk}} = -0.26 \pm 0.04$ . The errors here are likely underestimated, as we have not accounted for the correlations when using the same methods in this treatment. However, the results are instructive in that they demonstrate our specific choice of adopted scales is not highly biased.

The propagated observational errors are of order 0.01 to 0.03 dex for those indicators not using [O II]; for the [O II]-based results, the observational errors are of order 0.04 to 0.05 dex. The major contributors to the uncertainties in all of our analyses are the intrinsic dispersions expected when calculating  $\Delta\epsilon(\text{O})$  (see Table 3). While the offsets about the direct method  $\Delta\epsilon(\text{O})$  values (used to calculate  $\sigma_{\Delta\epsilon(\text{O})}$  in Table 3) are not strongly correlated for our adopted scales, we have not done a full assessment of this for the larger sample of reliable scales.

The *absolute* abundances from SEL scales can have significant systematic uncertainties. However, a representative abundance comes from the N2[ $\equiv I([\text{N II}] 6584)/I(\text{H}\alpha)$ ] scale of Pettini & Pagel (2004), which gives  $\epsilon(\text{O})_{\text{EHR1}} = 8.35 \pm 0.15$  and  $\epsilon(\text{O})_{\text{disk1}} = 8.63 \pm 0.15$  (where the errors are based on the dispersion of this scale about the direct method abundances from the literature sample discussed above). The full range of median abundances predicted for EHR1 by our adopted scales are  $\epsilon(\text{O})_{\text{EHR1}} = 8.24$  to 8.49.

#### 4. THE METALLICITY OF THE THICK DISK OF NGC 4013

The thick disk H II region NGC 4013 EHR1 probes gas at  $z = 860$  pc above the plane of this galaxy that is illuminated and energized by a cluster of young, hot stars (based on the photometric properties and  $\text{H}\alpha$  strength; see Paper II). This gas has an abundance a factor of  $\approx 2$  (0.3 dex) lower than that of the disk of NGC 4013. The disk gas in NGC 4013 has an abundance consistent with that of the local Milky Way disk, which is approximately “solar”,  $\epsilon(\text{O})_{\odot} = 8.72$  (Steffen et al. 2015). The low metallicity of the thick disk gas illuminated by these OB stars must therefore either represent (a) low-metallicity gas that has not mixed with material recently ejected from the disk, or (b) an admixture of recent fountain-ejected gas with very low metallicity material. It cannot be pure ejected disk gas given its low abundance.

The interstellar thick disk of NGC 4013, like many spiral galaxies, shows strong evidence for the presence of gas lifted from the midplane, perhaps through an active galactic fountain (although the hydraulic jump mechanism would lead to similar structure for our purposes). This evidence includes its observed multiphase structure (Rueff et al. 2013), which requires continuous energy input, the near co-rotation of the thick disk with gas in the plane (Zschaechner & Rand 2015), and the presence of significant amounts of dust (as the dust almost certainly originates in the disk; Rueff et al. 2013). And yet, given the low metallicity of gas at  $z = 860$  pc, the thick disk

**Table 4.** NGC 4013 EHR1 Abundance Summaries

Quantity	N2 [PP04]	O3N2 [M13]	O3 [C17]	Combined
$\epsilon(\text{O})_{\text{EHR1}}$	$8.35 \pm 0.15$	$8.43 \pm 0.15$	$8.38 \pm 0.17$	...
$\Delta\epsilon(\text{O})_{\text{disk 1}}$	$-0.26 \pm 0.17$	$-0.34 \pm 0.15$	$-0.40 \pm 0.18$	$-0.32 \pm 0.09$
$\Delta\epsilon(\text{O})_{\text{disk 2}}$	$-0.24 \pm 0.17$	$-0.22 \pm 0.15$	$-0.28 \pm 0.18$	$-0.24 \pm 0.10$

NOTE—The abundances and abundance offsets are given for the adopted SEL scales. The method and references for the calibration are given in the column headers. The  $\Delta\epsilon(\text{O})$  results are also given for a combined or joint result for each reference region. The errors are at 68% confidence.

gas in this galaxy cannot be pure ejected material; it must include a contribution from lower-metallicity gas.

Gas accreted directly as a cold stream from the IGM would have an extremely low metallicity, but such matter is likely to be heated to very high temperatures and held up in the corona of a low-redshift galaxy like NGC 4013 (e.g., Birnboim & Dekel 2003; van de Voort et al. 2011; Nelson et al. 2013, 2016). It is also unlikely that directly-accreting matter would be deposited into the thick disk at a projected radial distance of  $R \approx 2.5$  kpc from this galaxy’s center, especially if that gas has any initial angular momentum relative to the disk. (EHR1 has a velocity similar to that of the diffuse ionized and warm neutral gas at its position, so its rotation is not at odds with that of galactic fountain-driven gas.) The same argument makes it unlikely the low-metallicity nebula NGC 4013 EHR1 is tracing gas from an accreted dwarf satellite (the “bulls-eye” problem of Peek 2009). Though there is evidence for a major merger several Gyr ago (Wang et al. 2015) based on NGC 4013’s prodigious warp (Bottema 1996; Zschaechner & Rand 2015) and recently-discovered stellar stream (Martínez-Delgado et al. 2009), the probability of any gas from that merger landing within  $R \approx 2.5$  kpc of the center of NGC 4013 is small. (And finding it there would be even less likely since thick disk gas is returned to the plane in  $\sim 100$  Myr. Thus any material from an accreted dwarf would not find itself  $z \approx 1$  kpc above the midplane for very long.)

More likely is that any newly-acquired, low-metallicity matter is subsumed into the hot, massive corona of the galaxy and accreted onto the disk at a later time. The coronal matter must be cooled to bring it to the low  $z$ -heights and cool, dense conditions we observe. If the corona does have a low metallicity (in this case,  $\lesssim 1/2$  solar), cooling it may be problematic, as the efficacy of thermal instabilities in low-metallicity coronal gas is debated (Binney et al. 2009). However, such

cooling may be made possible by fountain-induced accretion<sup>6</sup> (Marinacci et al. 2010, 2012; Marasco et al. 2012). These models postulate that cold, metal-rich gas ejected from the disk can mix with hot, metal-poor coronal gas, enhancing its cooling, which causes the coronal gas to accrete onto the disk. However, our measured  $\Delta\epsilon(\text{O}) \approx -0.3$  dex between the thick and thin disk material in NGC 4013 is larger than these models are currently able to reproduce. If we assume the coronal material is pristine with no metals (an extreme model), equal amounts of coronal and fountain material would need to be mixed in order to produce the observed metallicity offset between EHR1 and the disk. For a higher-metallicity corona, a larger fraction of cooled coronal material is required. The fountain-driven accretion models predict that condensed coronal material will only contribute  $\approx 10 - 20\%$  of the total mass of extraplanar gas (Marasco et al. 2012), although such cooling can be more effective in lower-temperature coronae (Armillotta et al. 2016). Very recent simulations (Gritton et al. 2017) of metal-poor clouds flowing through a *metal-rich* corona show promise for condensing a larger amount of material, but it is not yet clear if they translate to the situation appropriate for NGC 4013.

One could imagine the low metallicity of the gas in EHR1 could be the result of the collision of a low-metallicity HVC with the disk (Franco et al. 1988; Lepine & Duvert 1994; Lockman et al. 2008; Park et al. 2016, e.g.,). In this case, the HVC material itself would provide the low-metallicity gas. This is somewhat different from direct accretion if HVCs represent material condensed from the hot, metal-poor corona and thus have relatively low angular momentum. It would still

<sup>6</sup> Although, given how the mechanism works, metal rich gas ejected through any mechanism (e.g., through a hydraulic jump) should provide similar results.

be unusual to observe this process directly given the timescales involved, but not unheard of (e.g., Lockman et al. 2008). Such a collision could be partially responsible for triggering the formation of dense clouds in the thick disk and ultimately the stars that power NGC 4013 EHR1 (e.g., Martos & Cox 1998). The nature and formation of the stars underlying EHR1 are discussed in Paper II.

## 5. VERTICAL ABUNDANCE GRADIENTS IN SPIRAL GALAXIES

### 5.1. *The Literature Sample of Thick Disk H II Regions*

Previous metallicity determinations are available for two extraplanar nebulae in the dwarf galaxy NGC 55 (Tüllmann et al. 2003) and for three nebulae in two massive spirals undergoing stripping (Stein et al. 2017). We have re-derived  $\Delta\epsilon(\text{O})$  for each of these, using the line intensities provided in the original references and following the approach described in §3.2. Our results comparing each extraplanar nebula in these galaxies with their respective disks are given in Table 5.

For the extraplanar H II regions recently presented by Stein et al. (2017) in two massive spiral galaxies, our calculations of  $\Delta\epsilon(\text{O})$  are in reasonable agreement with their determinations (within 0.1 dex, the typical error in our assessments). These nebulae in NGC 3628 and NGC 4522 are plausibly associated with tidally- or ram pressure-stripped gas about these group (NGC 3628) and cluster galaxies (NGC 4522).

For the H II regions seen above the plane of NGC 55 we find significantly different values for the absolute abundances than the original publication (Tüllmann et al. 2003), and our values imply a different sign for  $\Delta\epsilon(\text{O})$ . Our analyses of the H II regions in NGC 55 yield higher abundances in the two extraplanar H II regions than the single disk region in the Tüllmann et al. (2003) spectroscopy. Our assessments of the abundance of the reference disk H II region range from  $\epsilon(\text{O}) = 8.1 - 8.3$ . For comparison Tüllmann et al. (2003) calculated  $\epsilon(\text{O}) = 8.05 \pm 0.10$  using the direct method for the disk H II region. Kudritzki et al. (2016) derived  $\epsilon(\text{O}) \approx 8.32 \pm 0.03$  as the central abundance of NGC 55 based on measurements of the atmospheres of blue supergiants. Thus the absolute abundance we derive for the disk reference is consistent with the range of likely values. Our determinations of the abundances for the extraplanar H II regions cover  $8.1 \lesssim \epsilon(\text{O}) \lesssim 8.7$ . For the extraplanar regions, every scale denoted “reliable” in Table 3 yields a higher abundance than the disk H II region when using the same scale.

The difference in our results for NGC 55 compared with those of Tüllmann et al. (2003) are understand-

able given the advances in understanding SEL methods and their limitations since the original publication. Tüllmann et al. used the M91 (McGaugh 1991) calibration of  $R_{23}$  to derive absolute abundances. When using  $R_{23}$ , these nebulae are in a region of some ambiguity as to the correct choice of abundance from this indicator (Kewley & Ellison 2008). At the time that Tüllmann et al. derived their metallicities, the tools for assessing which branch to adopt for this double-valued indicator were less robust.

Extraplanar H II regions in the two massive spirals NGC 3628 and NGC 4522 show modest or no abundance offsets relative to their disks. Our results for these galaxies are consistent with the conclusions reached by Stein et al. (2017). In particular, the nebula at  $z \approx 1.4$  from the midplane of NGC 4522 is projected onto extraplanar H I identified as matter being stripped from the disk via the ram pressure interaction with the intracluster medium of the Virgo cluster in the maps of Kenney et al. (2004). Stein et al. (2017) note the extraplanar H II regions in NGC 3628 are projected onto an H I filament seen in the maps of Wilding et al. (1993) that has been identified as a tidal feature due to the interaction of this galaxy with its neighbor NGC 3627. Thus, the extraplanar H II regions may plausibly arise in gas stripped from both of the galaxies, and they represent fundamentally different phenomena than the extraplanar H II regions in NGC 55 and NGC 4013.

The spiral galaxy NGC 4522 resides in the Virgo cluster; direct imaging shows spectacular evidence for ram pressure-stripping of gas from the disk (Abramson & Kenney 2014). The extraplanar H II region measured in this galaxy is associated with this material that seems to clearly have an origin in the disk of that galaxy (Stein et al. 2017). We derive a joint abundance offset between the two disk H II regions observed and the single extraplanar H II region of  $\Delta\epsilon(\text{O}) = -0.03 \pm 0.07$  (68% confidence), consistent with no offset. This is as expected for material recently stripped from the disk.

In the case of NGC 3628 (part of the Leo Triplet of galaxies), two extraplanar H II regions are seen at  $z \approx 3$  kpc in close proximity to one another. Stein et al. note that these H II regions are likely associated with a filament of H I at similar velocities that likely represents tidal material due to an interaction of NGC 3628 with its neighbor NGC 3627 (Wilding et al. 1993). There are hints that the filament may have arisen in the outer parts of NGC 3628 (Stein et al. 2017), but they seem inconclusive. Compared with the single disk H II region measured in that galaxy, we find offsets of  $\Delta\epsilon(\text{O}) = -0.17 \pm 0.10$  and  $-0.05 \pm 0.11$  (68% confidence). If one assumes a single abundance offset is appropriate, the

**Table 5.** Extraplanar H II Region Abundance Offsets

Galaxy	Nebula ID	$z$ (pc)	$\Delta\epsilon(\text{O})$	Reference
NGC 4013	1	0.9	$-0.32 \pm 0.09$	This work
NGC 55	1	1.1	$+0.24 \pm 0.12$	Tüllmann et al. (2003)
NGC 55	2	2.2	$+0.29 \pm 0.12$	Tüllmann et al. (2003)
NGC 3628	2	2.8	$-0.17 \pm 0.10$	Stein et al. (2017)
NGC 3628	3	3.0	$-0.05 \pm 0.11$	Stein et al. (2017)
NGC 4522	1	1.4	$-0.03 \pm 0.07$	Stein et al. (2017)

NOTE—The nebular IDs are those reported in the original references. All abundance offsets  $\Delta\epsilon(\text{O})$  are derived anew using the intensities reported in the original references. Where more than one disk reference region is available (for NGC 4013 and NGC 4522), the values for  $\Delta\epsilon(\text{O})$  represent the joint distribution. The medians of the distributions are given along with errors representing 68% confidence.

joint distribution implies  $\Delta\epsilon(\text{O}) = -0.12 \pm 0.07$ . There is a hint that the abundances of these H II regions may have a slightly lower abundance than the disk, but the hint is not robust at the 95% level.

While the extraplanar regions tracing stripped material have abundances consistent with the disks of those galaxies, the extraplanar nebulae in the dwarf galaxy NGC 55 have higher abundances than the disk. The extraplanar H II regions in NGC 55 seem to be connected with supershells produced by vigorous star formation-driven feedback Tüllmann et al. (2003). Assuming the recently-determined distance to NGC 55 ( $D = 2.34$  Mpc; Kudritzki et al. 2016), these are projected  $z \approx 1.1$  and 2.2 kpc from the midplane (compared with the previous estimate of  $z \approx 0.8$  and 1.5 kpc). Ferguson et al. (1996) first identified these H II regions based on H $\alpha$  imaging. The lower H II region is found within a large supershell on the northern side of the galaxy, while the upper one is found at the end of a long ( $\sim 1.5$  kpc) filament of H $\alpha$  emission on the southern side of the galaxy.

Both Ferguson et al. (1996) and Tüllmann et al. (2003) have speculated whether the processes that produce these large H $\alpha$ -emitting structures in NGC 55 may have played a role in triggering the formation of stars in the thick disk of this galaxy. This is consistent with our  $\Delta\epsilon(\text{O})$  determinations: if feedback-driven outflows are the ultimate source of the gas emitting in these nebulae, one may expect that gas to be more metal rich than the disk if there has been little mixing with more metal-poor material.

### 5.2. Vertical Abundance Gradients in Context

We compare the implied gradient in abundances for the complete literature sample of extraplanar H II region abundance determinations (Tüllmann et al. 2003; Stein

et al. 2017) in Figure 4. We also include results from the Milky Way intermediate and high velocity clouds (IVCs and HVCs; Wakker 2001; Richter et al. 2001; Sembach et al. 2004; Hernandez et al. 2013; Fox et al. 2016). In this context, we define the gradient simply as  $\Delta\epsilon(\text{O})/z$  for each H II region or cloud. The full sample of extraplanar H II region abundances shown in Figure 4 paint a mixed picture of vertical abundance gradients in galaxies. Given the small sample size, and particularly given the variety of origins plausibly attributable to each, it is not clear what overarching conclusions can yet be drawn.

The factor of two abundance offset between the extraplanar H II region EHR1 and the disk of NGC 4013 is reminiscent of the difference seen between some Galactic HVCs and the Milky Way’s disk (Wakker 2001; Barentine 2013). However, the HVCs tend to be much further from the Galactic disk than  $z \sim 1$  kpc (Lehner & Howk 2011; Lehner et al. 2012), giving smaller gradients in Figure 4. The Galactic IVCs are a better match to the height probed by NGC 4013 EHR1 (Wakker 2001), and they are the closest Milky Way analogs to the massive, dusty clouds seen in direct imaging of edge-on galaxies (Howk & Savage 1999, 2000; Rueff et al. 2013). Only one IVC, IV21 at  $|z| \approx 285$  pc from the plane of the Milky Way, has a low metallicity (measured principally using S) with  $\epsilon(\text{S}) = -0.43 \pm 0.12$  (Hernandez et al. 2013). All of the other clouds within the first few kpc are consistent with zero metallicity gradient. The metallicity gradients in the thick disk of the Milky Way are generally quite small within  $z \sim 1 - 3$  kpc.

The gradients represented by EHR1 in NGC 4013 and IV21 in the Milky Way are the largest observed, in part because they are at small  $z$ . And, indeed, this is in part what makes both examples so interesting. Figure 4



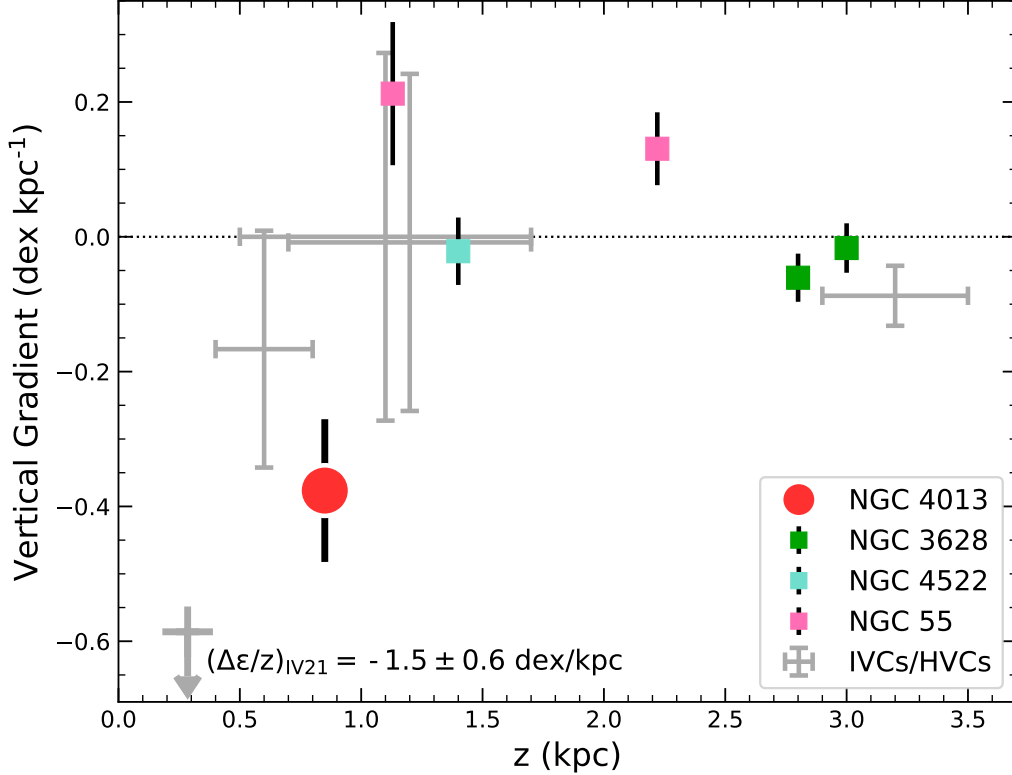


**Figure 4.** Abundance gradients,  $\Delta\epsilon(O)/z$ , implied by the existing sample of extraplanar H II regions (Tüllmann et al. 2003; Stein et al. 2017) as a function of height from the midplane. The  $\Delta\epsilon(O)$  values have been derived for all regions as for EHR1; thus the values used here may differ from those in the original references. In particular, the extraplanar H II regions in NGC 55 have a positive offset relative to the disk (contrary to earlier results Tüllmann et al. 2003). The systems shown by squares (in NGC 3628 and NGC 4522) likely arise in stripped gas, perhaps from the host galaxy. The extraplanar nebulae in NGC 55 are likely associated with gas participating in a galactic fountain circulation. The high- $z$  nebula in NGC 4013 may be a mixture of fountain gas and gas much lower metallicity. Also shown are results from Milky Way IVCs (Wakker 2001; Richter et al. 2001; Sembach et al. 2004; Hernandez et al. 2013) and one HVC (the Smith Cloud; Fox et al. 2016). Other HVCs with abundance measurements are at much larger  $z$ . The IVC IV21 (Hernandez et al. 2013) resides at a value of  $-1.5 \pm 0.6$  on the vertical scale (with  $\Delta\epsilon \approx -0.4$  and  $|z| \approx 285$  pc); we place it at an arbitrary position vertically in this figure.

demonstrates that the scales for metallicity changes can be much smaller in the vertical than the radial directions in spiral galaxies, with the caveat that we cannot yet demonstrate there are true gradients as opposed to random mixtures of different metallicity gas. There are several other galaxies with extraplanar H II regions suitable for spectroscopy such as that described here, and these may help clarify the picture.

The interstellar thick disks of galaxies are complex admixtures of gas having different origins. Our results suggest large metallicity inhomogeneities exist on scales of only 100s of pc (certainly between the mid-plane and the thick disk, but even within the thick disk). In addition, the low metallicity of EHR1 relative to the disk of NGC 4013 and of IV21 relative to the Milky

Way’s disk (Hernandez et al. 2013) suggest the fueling of galactic disks by low-metallicity gas is robust at low-redshift, which has corresponding implications for chemical evolution calculations. The observational questions moving forward will be whether such low-metallicity inclusions are common in spiral galaxies (e.g., Figure 4) and whether the metallicity variations are organized or stochastic.

Ultimately our favored model for explaining the low abundance seen in the thick disk of NGC 4013 is some form of induced accretion (Marinacci et al. 2010; Marasco et al. 2012; Fraternali 2017). However, if such large abundance offsets are common, more work will need to be done to understand if the cooling efficiency of that model can be increased.

## 6. SUMMARY

We have presented optical spectroscopy of an H II region in the thick disk of the nearby spiral galaxy NGC 4013. The nature of this H II region and its underlying stars is discussed in Paper II. Here we consider the relative abundance of this nebula compared with the disk in order to understand the nature of the thick disk in spiral galaxies. Our principle conclusions are as follows.

1. The emission line spectrum of NGC 4013 EHR1 is generally consistent with those of H II regions in the disks of spiral galaxies. Thus, it is a relatively luminous H II region located  $z = 860$  pc above the plane of this spiral galaxy. The  $H\alpha$  luminosity implies the presence of the equivalent of  $\sim 6$  O7 V stars (see Paper II).
2. The abundance of EHR1 is a factor of  $\approx 2$  below that of the disk of NGC 4013 (as assessed using two H II regions in the midplane). Our preferred value for the abundance offset is  $\Delta\epsilon(\text{O})_{\text{EHR1-disk1}} = -0.32 \pm 0.09$ .
3. The low abundance of EHR1 implies significant amounts of low-metallicity gas have been mixed into the thick disk of NGC 4013. This is particularly interesting given the presence of large amounts of material expelled from the disk as part

of an active galactic fountain or hydraulic jump in this galaxy.

4. A small sample of measurements of vertical abundance gradients from extraplanar H II regions and extraplanar clouds in the Milky Way does not yet show consistent trends. There are examples of positive, negative, and no abundance gradients with  $z$ -height. It is not clear if the gradients that are seen are organized or stochastic.

JCH recognizes the hospitality of the Instituto de Astrofísica, Pontificia Universidad Católica de Chile during the writing of this work. Portions of this work has been supported by NASA through grant NNX10AE87G as well as the NSF through grant AST-1212012. It makes use of data collected at the LBT, an international collaboration among institutions in the United States, Italy and Germany. LBT Corporation partners are: The University of Arizona on behalf of the Arizona Board of Regents; Istituto Nazionale di Astrofisica, Italy; LBT Beteiligungsgesellschaft, Germany, representing the Max-Planck Society, The Leibniz Institute for Astrophysics Potsdam, and Heidelberg University; The Ohio State University, and The Research Corporation, on behalf of The University of Notre Dame, University of Minnesota and University of Virginia.

*Software:* Astropy (Price-Whelan et al. 2018), Matplotlib (Hunter 2007), pyMCZ (Bianco et al. 2016)

*Facilities:* LBT(MODS), HST(WFPC2), WIYN

## REFERENCES

- Abramson, A., & Kenney, J. D. P. 2014, *AJ*, 147, 63  
 Armillotta, L., Fraternali, F., & Marinacci, F. 2016, *MNRAS*, 462, 4157  
 Barentine, J. C. 2013, PhD thesis, The University of Texas at Austin  
 Bauermeister, A., Blitz, L., & Ma, C.-P. 2010, *ApJ*, 717, 323  
 Berg, D. A., Skillman, E. D., Croxall, K. V., et al. 2015, *ApJ*, 806, 16  
 Bianco, F. B., Modjaz, M., Oh, S. M., et al. 2016, *Astronomy and Computing*, 16, 54  
 Binney, J., Nipoti, C., & Fraternali, F. 2009, *MNRAS*, 397, 1804  
 Birnboim, Y., & Dekel, A. 2003, *MNRAS*, 345, 349  
 Bizyaev, D., Walterbos, R. A. M., Yoachim, P., et al. 2017, *ApJ*, 839, 87  
 Boettcher, E., Zweibel, E. G., Gallagher, III, J. S., & Benjamin, R. A. 2016, *ApJ*, 832, 118  
 Bottema, R. 1996, *A&A*, 306, 345  
 Bregman, J. N. 1980, *ApJ*, 236, 577  
 Bresolin, F. 2007, *ApJ*, 656, 186  
 Bresolin, F., Gieren, W., Kudritzki, R.-P., et al. 2009, *ApJ*, 700, 309  
 Cappellari, M. 2017, *MNRAS*, 466, 798  
 Croxall, K. V., Pogge, R. W., Berg, D. A., Skillman, E. D., & Moustakas, J. 2015, *ApJ*, 808, 42  
 Croxall, K. V., Pogge, R. W., Berg, D. A., Skillman, E. D., & Moustakas, J. 2016, *ApJ*, 830, 4  
 Curti, M., Cresci, G., Mannucci, F., et al. 2017, *MNRAS*, 465, 1384  
 Dettmar, R.-J. 1990, *A&A*, 232, L15  
 Ferguson, A. M. N., Wyse, R. F. G., & Gallagher, J. S. 1996, *AJ*, 112, 2567  
 Fox, A. J., Lehner, N., Lockman, F. J., et al. 2016, *ApJL*, 816, L11

- Franco, J., Tenorio-Tagle, G., Bodenheimer, P., Rozyczka, M., & Mirabel, I. F. 1988, *ApJ*, 333, 826
- Fraternali, F. 2017, in *Astrophysics and Space Science Library*, Vol. 430, *Astrophysics and Space Science Library*, ed. A. Fox & R. Davé, 323
- Fraternali, F., & Binney, J. J. 2006, *MNRAS*, 366, 449
- Fraternali, F., Oosterloo, T., Sancisi, R., & van Moorsel, G. 2001, *ApJL*, 562, L47
- Fraternali, F., & Tomassetti, M. 2012, *MNRAS*, 426, 2166
- García-Burillo, S., Combes, F., & Neri, R. 1999, *A&A*, 343, 740
- Gritton, J. A., Shelton, R. L., & Galyardt, J. E. 2017, *ApJ*, 842, 102
- Heald, G. H., Rand, R. J., Benjamin, R. A., Collins, J. A., & Bland-Hawthorn, J. 2006, *ApJ*, 636, 181
- Hernandez, A. K., Wakker, B. P., Benjamin, R. A., et al. 2013, *ApJ*, 777, 19
- Howk, J. C. 2012, in *EAS Publications Series*, Vol. 56, *EAS Publications Series*, ed. M. A. de Avezil, 291–298
- Howk, J. C., Rueff, K. M., Lehner, N., Croxall, K. V., & Savage, B. D. 2018, *ApJ*, submitted (Paper II)
- Howk, J. C., & Savage, B. D. 1999, *AJ*, 117, 2077
- . 2000, *AJ*, 119, 644
- Hunter, J. D. 2007, *Computing In Science & Engineering*, 9, 90
- Kenney, J. D. P., van Gorkom, J. H., & Vollmer, B. 2004, *AJ*, 127, 3361
- Kennicutt, Jr., R. C. 1983, *ApJ*, 272, 54
- Kewley, L. J., & Dopita, M. A. 2002, *ApJS*, 142, 35
- Kewley, L. J., & Ellison, S. L. 2008, *ApJ*, 681, 1183
- Kobulnicky, H. A., & Kewley, L. J. 2004, *ApJ*, 617, 240
- Kudritzki, R. P., Castro, N., Urbaneja, M. A., et al. 2016, *ApJ*, 829, 70
- Lehner, N., & Howk, J. C. 2011, *Science*, 334, 955
- Lehner, N., Howk, J. C., Thom, C., et al. 2012, *MNRAS*, 424, 2896
- Lepine, J. R. D., & Duvert, G. 1994, *A&A*, 286, 60
- Lockman, F. J., Benjamin, R. A., Heroux, A. J., & Langston, G. I. 2008, *ApJL*, 679, L21
- López-Sánchez, Á. R., Dopita, M. A., Kewley, L. J., et al. 2012, *MNRAS*, 426, 2630
- Maiolino, R., Nagao, T., Grazian, A., et al. 2008, *A&A*, 488, 463
- Marasco, A., Fraternali, F., & Binney, J. J. 2012, *MNRAS*, 419, 1107
- Marinacci, F., Binney, J., Fraternali, F., et al. 2010, *MNRAS*, 404, 1464
- Marinacci, F., Fraternali, F., Binney, J., et al. 2012, in *European Physical Journal Web of Conferences*, Vol. 19, *European Physical Journal Web of Conferences*, 08008
- Marino, R. A., Rosales-Ortega, F. F., Sánchez, S. F., et al. 2013, *A&A*, 559, A114
- Martínez-Delgado, D., Pohlen, M., Gabany, R. J., et al. 2009, *ApJ*, 692, 955
- Martos, M. A., & Cox, D. P. 1998, *ApJ*, 509, 703
- McGaugh, S. S. 1991, *ApJ*, 380, 140
- Nelson, D., Genel, S., Pillepich, A., et al. 2016, *MNRAS*, 460, 2881
- Nelson, D., Vogelsberger, M., Genel, S., et al. 2013, *MNRAS*, 429, 3353
- Park, G., Koo, B.-C., Kang, J.-h., et al. 2016, *ApJL*, 827, L27
- Peek, J. E. G. 2009, *ApJ*, 698, 1429
- Peek, J. E. G., Heiles, C., Putman, M. E., & Douglas, K. 2009, *ApJ*, 692, 827
- Pérez-Montero, E., & Contini, T. 2009, *MNRAS*, 398, 949
- Pettini, M., & Pagel, B. E. J. 2004, *MNRAS*, 348, L59
- Pogge, R. W., Atwood, B., Brewer, D. F., et al. 2010, in *Proc. SPIE*, Vol. 7735, *Ground-based and Airborne Instrumentation for Astronomy III*, 77350A
- Price-Whelan, A. M., Sipőcz, B. M., Günther, H. M., et al. 2018, *ArXiv e-prints*, arXiv:1801.02634
- Rand, R. J. 1996, *ApJ*, 462, 712
- Rand, R. J., Kulkarni, S. R., & Hester, J. J. 1990, *ApJL*, 352, L1
- Richter, P., Sembach, K. R., Wakker, B. P., et al. 2001, *ApJ*, 559, 318
- Rueff, K. M., Howk, J. C., Pitterle, M., et al. 2013, *AJ*, 145, 62
- Rumstay, K. S. 1984, PhD thesis, Ohio State University, Columbus.
- Sánchez-Blázquez, P., Peletier, R. F., Jiménez-Vicente, J., et al. 2006, *MNRAS*, 371, 703
- Sandstrom, K. M., Peek, J. E. G., Bower, G. C., Bolatto, A. D., & Plambeck, R. L. 2007, *ApJ*, 667, 1161
- Schlafly, E. F., & Finkbeiner, D. P. 2011, *ApJ*, 737, 103
- Sembach, K. R., Wakker, B. P., Tripp, T. M., et al. 2004, *ApJS*, 150, 387
- Shapiro, P. R., & Field, G. B. 1976, *ApJ*, 205, 762
- Steffen, M., Prakashavičius, D., Caffau, E., et al. 2015, *A&A*, 583, A57
- Stein, Y., Bomans, D. J., Ferguson, A. M. N., & Dettmar, R.-J. 2017, *A&A*, 605, A5
- Struck, C., & Smith, D. C. 2009, *MNRAS*, 398, 1069
- Tüllmann, R., Rosa, M. R., Elwert, T., et al. 2003, *A&A*, 412, 69
- Tully, R. B., Shaya, E. J., Karachentsev, I. D., et al. 2008, *ApJ*, 676, 184
- van de Voort, F., Schaye, J., Booth, C. M., Haas, M. R., & Dalla Vecchia, C. 2011, *MNRAS*, 414, 2458

- Wakker, B. P. 2001, *ApJS*, 136, 463
- Walterbos, R. A. M. 1991, in *IAU Symposium*, Vol. 144, The Interstellar Disk-Halo Connection in Galaxies, ed. H. Bloemen, 223–232
- Wang, J., Hammer, F., Puech, M., Yang, Y., & Flores, H. 2015, *MNRAS*, 452, 3551
- Werk, J. K., Putman, M. E., Meurer, G. R., & Santiago-Figueroa, N. 2011, *ApJ*, 735, 71
- Wilding, T., Alexander, P., & Green, D. A. 1993, *MNRAS*, 263, 1075
- Zschaechner, L. K., & Rand, R. J. 2015, *ApJ*, 808, 153